Journal of Microscopy

Journal of Microscopy, Vol. 261, Issue 2 2016, pp. 130–147 doi: 10.1111/jmi.12156
Received 24 April 2014; accepted 21 June 2014

Soft X-ray spectromicroscopy for speciation, quantitation and nano-eco-toxicology of nanomaterials

J.R. LAWRENCE*, G.D.W. SWERHONE*, J.J. DYNES†, D.R. KORBER‡ & A.P. HITCHCOCK§
*Environment Canada, Saskatoon, SK, Canada
†Canadian Light Source Inc., University of Saskatchewan, SK, Canada
‡Food and Bioproducts Sciences, University of Saskatchewan, Saskatoon, SK, Canada
§Department of Chemistry and Chemical Biology, McMaster University, Hamilton, ON, Canada

Key words. Bacteria, biofilms, carbon nanotubes, metals, nanomaterials/nanoparticles, Scanning Transmission X-Ray Microscopy, STXM.

Summary

There is a critical need for methods that provide simultaneous detection, identification, quantitation and visualization of nanomaterials at their interface with biological and environmental systems. The approach should allow speciation as well as elemental analysis. Using the intrinsic X-ray absorption properties, soft X-ray scanning transmission X-ray spectromicroscopy (STXM) allows characterization and imaging of a broad range of nanomaterials, including metals, oxides and organic materials, and at the same time is able to provide detailed mapping of biological components. Thus, STXM offers considerable potential for application to research on nanomaterials in biology and the environment. The potential and limitations of STXM in this context are discussed using a range of examples, focusing on the interaction of nanomaterials with microbial cells, biofilms and extracellular polymers. The studies outlined include speciation and mapping of metal-containing nanomaterials (Ti, Ni, Cu) and carbon-based nanomaterials (multiwalled carbon nanotubes, C_{60} fullerene). The benefits of X-ray fluorescence detection in soft X-ray STXM are illustrated with a study of low levels of Ni in a natural river biofilm.

Introduction

Nanomaterials are those materials with at least one dimension less than 100 nm, a factor which provides a broad range of special properties that are being exploited in industry, medicine, manufacturing and technology development. However, these properties also give rise to a range of concerns, particularly when, as is inevitably the case, these materials are intentionally or accidentally released to the environment (Boxall *et al.*, 2007; Handy *et al.*, 2008; Petersen *et al.*, 2011). Initially, the major nanomaterials of concern were metallic, perhaps with organic coatings. However, this has rapidly changed to include a range of carbon-based and complex composite nanomaterials presenting additional challenges for characterization, detection and ecotoxicological study.

Early papers on the assessment of nanomaterials focused on the use of infrared (IR), nuclear magnetic resonance (NMR), ultraviolet-visible, scanning probe and electron beam microscopies [transmission electron microscopy (TEM), scanning electron microscopy (SEM)], as well as environmental SEM (ESEM), and wet-SEM (Domingos *et al.*, 2009; Tiede *et al.*, 2009). UV-visible, Raman and near-infrared spectromicroscopy techniques have also been applied although they lack the spatial resolution required to detect and characterize individual nanomaterials (Berciaud *et al.*, 2007; Kim *et al.*, 2007; Miyata *et al.*, 2008). Although many of these techniques offer specific advantages for the study of particular nanomaterials, they may lack the capacity for wet samples, cause radiation damage (as in the case of electron beam techniques) or lack the necessary chemical sensitivity (as in the case of scanning probe technologies). Some approaches may only be effective for metal or metal oxide nanoparticles (NPs). Methods such as electron beam techniques can be costly, time-consuming and restrictive in terms of sample and object number. Nanomaterials in biological systems have been investigated using the CytoViva Hyperspectral Imaging System, a dark field optical microscope which illuminates the sample and then captures the scattered light (Badireddy *et al.*, 2012). In this system, analyses are based on the application of visible and near-infrared spectroscopy to interpret the nature of materials in the sample. Thus, although there are a number of analytical techniques that may be applied to the study of nanomaterials, many of which have specific advantages, few offer the desired capacity

Correspondence to: A.P. Hitchcock, Department of Chemistry and Chemical Biology, McMaster University, Hamilton, ON L8S4M1, Canada. Tel: 1-905-525-9140, ext. 24729; fax: 1-905-521-2773; e-mail: aph@mcmaster.ca

for detection, speciation and quantitation of both metals and organics at high spatial resolution (Lawrence & Hitchcock, 2011; Lawrence *et al.*, 2012).

Synchrotron-based spectromicroscopy techniques are increasingly important tools for the analyses of environmental materials and contaminants (Bluhm *et al.*, 2006; Graf *et al.*, 2008; Neu *et al.*, 2010; Thieme *et al.*, 2008, 2010; Lawrence & Hitchcock, 2011; Piticharoenphun *et al.*, 2012; Muehe *et al.*, 2013; Novak *et al.*, 2013). A recent review (Hitchcock 2012) contains a complete bibliography of soft X-ray spectromicroscopy, which is regularly updated and available at http://unicorn.mcmaster.ca/xrm-biblio/xrm_bib.html. The fate and effects of nanomaterials in the environment and their toxicology involves microscopically variable chemical and biological interactions that should be analysed at high spatial resolution. Indeed, it may be viewed as essential to study the behaviour of NPs in a context that includes environmental interactions, with high resolution and at the appropriate scale. Soft X-ray scanning transmission X-ray spectromicroscopy (STXM) combines the chemical sensitivity of near-edge X-ray absorption fine structure spectroscopy with high spatial resolution. STXM is capable of mapping the biochemical composition of bacteria and biofilms at the subcellular scale (spatial resolution better than 30 nm) (Lawrence *et al.*, 2003), as well as speciation of metals (Dynes *et al.*, 2006a, b; Hitchcock *et al.*, 2009) and detection of organic contaminants (Dynes *et al.*, 2009; Lawrence *et al.*, 2014) in biofilms and other biological samples. Most STXM studies to date have been performed using 2D projection methods on suitably thin samples. Increasingly, 3D chemical distributions are being acquired using angle-scan computed spectrotomography (Johansson *et al.*, 2006, 2007; Hitchcock *et al.*, 2008b; Obst *et al.*, 2009; Schmid *et al.*, 2014). In this context, spectrotomography refers to tomographic measurements carried out in such a way as to provide explicit chemical mapping in 3D, which is achieved by using multiple photon energies in STXM. Similar 3D chemical mapping is also being achieved using hard X-ray tomography with X-ray fluorescence (XRF) detection (de Jonge *et al.*, 2010; Lombi *et al.*, 2011) although the spatial resolution is usually coarser and only elemental mapping is provided, as opposed to the chemical speciation (i.e. mapping specific chemical compounds) which STXM provides. STXM image sequences may be collected over a wide range of energies at the C 1s, O 1s and various metal 2p absorption edges. When these data sets are analysed using appropriate reference spectra, 2D and 3D quantitative component maps can be generated to visualize the nanomaterials and associated biological and mineral components. Thus, STXM is well suited to detect, speciate, quantify and observe nanomaterials and their interactions with biology in the environment. That said, STXM is not intended as a stand-alone technique or a replacement for other approaches which may offer specific and complementary information regarding nanomaterials. It is best able to contribute to understanding any given problem in the context of a correlative microscopies approach. Lawrence *et al.* (2003) described the application of STXM, confocal laser scanning microscopy (CLSM) and TEM to study microbial biofilms, combining a method that allowed greater penetration with those that provided higher resolution and chemical sensitivity.

STXM has been applied effectively to a range of studies focused on nanomaterials. Felten *et al.* (2006, 2007) applied STXM to study the electronic and structural properties of multiwalled carbon nanotubes (MWCNTs), showing that they could image isolated nanotubes and differentiate surface functional groups at the nanoscale. Rossouw *et al.* (2012) similarly showed that individual and bundles of single-walled carbon nanotubes (SWCNTs) could be investigated using electron energy loss spectroscopy in transmission electron microscope (TEM-EELS) and STXM-based X-ray absorption spectroscopy. In these studies, although more limited by radiation damage (Wang *et al.*, 2009a, b) and with lower energy resolution, TEM-EELS was shown to be highly complementary to STXM-near-edge X-ray absorption fine structure data (Felten *et al.*, 2006; Rossouw *et al.*, 2012). In general, it has been possible to examine purity, order and functionalization of carbon nanomaterials using STXM (Najafi *et al.*, 2008, 2010, 2012). STXM has also been applied in the study of naturally occurring nanomaterials, such as the membrane-bound magnetic NPs referred to as magnetosomes (Bazylinski & Frankel, 2004; Bazylinski *et al.*, 2013). For example, Lam *et al.* (2010) pioneered measurements of the X-ray magnetic circular dichroism of individual magnetosomes, whereas Kalirai *et al.* (2012, 2013) demonstrated anomalies in the orientation of magnetosome chains in *Magnetovibrio blakemorei* and also provided a rationale for their development. In a study of environmental fate and effects of metal NPs, Lawrence *et al.* (2012) applied STXM to speciate copper oxide NPs in a river biofilm community showing that for some metal nanomaterials, sorption to cells and exopolymers occurred in river biofilms with subsequent dissolution and resorption. This provided evidence important to understanding the chemodynamics and effects of metal NPs and how they may enter aquatic food webs. STXM may also be applied to studies of carbon nanotubes (CNTs) in an environmental context. For example, Lawrence *et al.* (2014) examined MWCNTs and SWCNTs that had been exposed to river water and developing river biofilms. Detailed, high-resolution STXM analyses showed that both types of CNTs underwent rapid surface modification with the development of distinct and different complex organic coatings, including protein, polysaccharide, lipid and calcium carbonate. In addition to using STXM in the transmission mode, samples may also be examined using low-energy XRF which improves detection relative to transmission (Hitchcock *et al.*, 2012). Indeed, this technique has been demonstrated to be effective for multielement mapping using a variety of samples (Gianoncelli *et al.*, 2009, 2013) including CoFe nanoparticles in mouse fibroblast samples (Marmorato *et al.*, 2011).

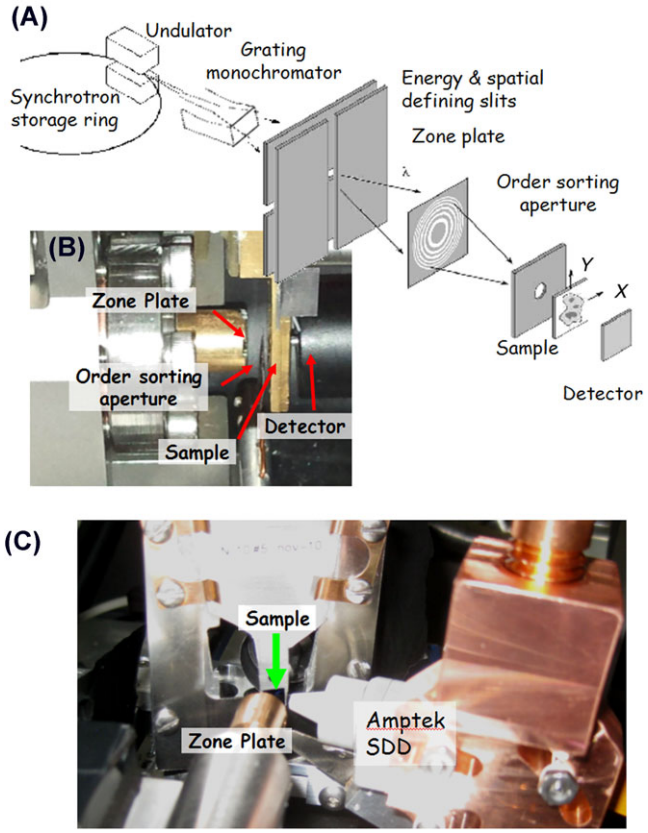

Fig. 1. (A) Schematic (not to scale) of the CLS 10ID1 beamline and scanning transmission X-ray microscope (STXM). The 10ID1 insertion device is an elliptically polarizing undulator. (B) Photograph of the microscope elements. (C) Photograph of the CLS ambient STXM equipped with an Amptek silicon drift detector used for X-ray fluorescence detection.

Soft X-ray STXM is particularly useful for studying the interactions of nanomaterials with biology because it uses the intrinsic spectral properties of the species themselves to provide detailed characterization of both the nanomaterials and the biological components. The spatial resolution (~30 nm) is about one order of magnitude better than conventional optical microscopy but several orders of magnitude worse than TEM, and also somewhat worse than superresolution optical microscopy (Giepmans, 2008; Patterson *et al.*, 2010). The chemical sensitivity is generally better than TEM, even if TEM-EELS is used. Although also limited in some applications due to the intrinsic damage that accompanies all ionization radiation probes, the amount of information per unit radiation damage in an STXM measurement is superior to TEM-EELS, the closest analytical equivalent, by several orders of magnitude (Hitchcock *et al.*, 2008a; Wang *et al.*, 2009a, b). Hard X-ray microscopies have a tremendous advantage over soft X-ray methods with respect to penetration through thick samples, which makes it easier to study systems in their natural state. However, the typical XRF methodology used for chemical analysis in hard X-ray microprobes only provides elemental sensitivity, unless XRF-yield X-ray absorption near-edge fine structure is carried out. In the context of nanomaterial–biology studies, the sensitivity of soft X-ray STXM to biology through the S 2p, C 1s, Ca 2p, N 1s and O 1s edges provides far more information about the biological aspects of these systems than hard X-ray microprobe or TEM. Luminescence labelling, particularly when combined with superresolution optical methods, provides far superior mapping of specific species than STXM can, but it is typically blind to identifying the unlabelled components of a complex system. As emphasized earlier and at the end of this paper, while STXM has some very attractive attributes when applied to studies of nanomaterials in a biological context, it is even more powerful when combined with other methods in a correlative microscopy approach.

In this paper, we discuss the STXM methodology using transmission and fluorescence modes and provide examples of applications with a focus on the interfaces between nanomaterials, bacteria and environmental biofilms. Some examples of correlative microscopy, combining STXM with CLSM, are included. Many details regarding the application of STXM and related techniques have also been summarized in recent comprehensive reviews (Neu *et al.*, 2010; Lawrence & Hitchcock, 2011; Hitchcock, 2012).

Experimental

Scanning transmission X-ray microscopy and data analysis

All of the data presented in this overview were measured using the ambient STXM[1] on beamline 10ID1 at the Canadian Light Source (CLS, Saskatoon, SK, Canada) (Kaznatcheev *et al.*, 2007). Figure 1(A) is a schematic of the beamline and STXM at the CLS (not to scale). CLS 10ID1 is an undulator beamline covering 130–2700 eV with fully tunable polarization. For normal transmission measurements, left circular polarization is used for energies below 1200 eV, whereas horizontally polarized light was used for the XRF measurements in order to minimize elastic scattering (Hitchcock *et al.*, 2012). Figure 1(B) is a photo of the sample region of the microscope as arranged for transmission mode detection. Figure 1(C) is a photo of the sample region of the microscope equipped with an Amptek silicon drift detector used for XRF detection. The details of the STXM instrument (Kilcoyne *et al.*, 2003) and its operation have been described elsewhere (Hitchcock, 2012). Monochromatic X-rays from the beamline illuminate a Fresnel zone plate lens which focuses monochromatic X-rays to a ~30-nm spot. An order sorting aperture is used to pass the first-order diffracted X-rays while blocking the zeroth order (undiffracted) light. The sample is positioned at the focal point

[1] From this point forward, CLS will have two STXM microscopes on the same beamline, which are distinguished by the labels, ambient-STXM (existing), and cryo-STXM (under construction at the time of writing this paper).

of the zone plate. Those X-rays that pass through the sample are detected in single photon counting mode using a detector consisting of a phosphor to convert soft X-rays to visible light and a high-performance photomultiplier to detect the visible photons. The zone plate (Center for X-ray Optics, LBNL) has a 25-nm outer zone width, 240 μm diameter and a 90-μm central stop. The order sorting aperture is 50 μm in diameter. Images at a single X-ray energy are measured by recording the transmitted X-ray intensity, $I(X, Y, E)$, at each pixel in a user-selected area of the sample which is raster scanned with a piezo scanning stage. Samples are measured in an environment of 0.15 atmospheres of He. Samples can be dry, mounted on 3-mm TEM grids or on silicon nitride or silicon X-ray transparent windows, or they can be hydrated, in which case the sample needs to be enclosed in a wet cell using either polyimide or silicon nitride windows. Transmission images were measured with a dwell time of 1 ms per pixel whereas XRF and X-ray Fluorescence detected X-ray absorption (XRF-XAS) images were recorded with various dwell times from 0.1 s (full XRF-XAS stacks) up to 10 s (for XRF maps at a single incident photon energy). Further details of the XRF detector and its operation have been presented elsewhere (Hitchcock *et al.*, 2012).

Properties of the nanomaterials used in the described experiments are given in Table 1. The general procedure used to prepare biofilm – NP samples was as follows. River biofilms were grown on polycarbonate slides for 50 days. The attached biofilms were then exposed to 1 mg mL^{-1} of the NP prepared in river water for either 5 min or 3 days, after which they were rinsed with sterile tap water (3×) to remove all but sorbed NP. Biofilm material was then aseptically scraped from the entire slide (11 cm^2) with a sterile silicone spatula and placed in a sterile 1-mL centrifuge tube. The sample was not homogenized as the goal was to look at biofilms in as intact a condition as possible. The samples for STXM analysis were prepared by deposition of 1–5 μL of the biofilm solution material onto Si_3N_4 windows (1 mm × 1 mm, thickness 100 nm on a 5 mm × 5 mm 200 μm thick chip, Norcada Inc., Edmonton, Canada). After the droplet was placed on the window, the sample was air-dried for a few minutes on the stage of a stereo microscope (Dynes *et al.*, 2006a, b). All samples were analysed by confocal laser microscopy (Bio-Rad MRC 1024, Zeiss, Jena, Germany) using the fluorescent stains, Syto9 (Molecular Probes, Eugene, OR, U.S.A.) and *Triticum vulgaris* lectin Tetramethylrhodamine isothiocyanate (TRITC) (Sigma, St. Louis, MI, U.S.A.), to visualize bacterial cells and exopolymer, respectively. This allowed the selection of representative biofilm areas which could be then systematically analysed using STXM.

STXM was performed at selected metal and C 1s edges on the CLS spectromicroscopy beamline (10ID-1). The beamline was operated at an energy resolving power, $E/\Delta E \geq 3000$. The as-measured transmitted signals were converted to optical densities (ODs, absorbance) using incident flux measured through regions of the window devoid of biofilm to correct for the absorbance by the silicon nitride window and other upstream optical components. After each analytical measurement, an image was recorded at 289 eV, an energy which readily visualizes radiation damage to polysaccharides, the most easily damaged chemical component. The polysaccharide signal in the extracellular matrix was reduced by less than 20% following beam exposure in the worst case of the measurements reported. The microscope energy scale was calibrated to an accuracy of ±0.05 eV using sharp gas phase signals, typically the Rydberg peaks of CO_2. STXM was used analytically by measuring image sequences at specific energies (Jacobsen *et al.*, 2000) or from image difference maps which are the difference of on- and off-resonance images (Dynes *et al.*, 2006a). Data analysis was performed using aXis2000 (Hitchcock, 2014)

Results and discussion

Toxicology of organic nanomaterials in the environment

Detection and characterization of CNTs. As is the case for many nanomaterials, TEM represents the gold standard for characterization of CNTs. Behaviour and interactions of nanotubes have been studied using traditional techniques, such as CLSM, TEM, and SEM (Rao *et al.*, 1997; Porter *et al.*, 2007). However, there are a range of methods that may be used to detect and characterize CNTs, such as EELS, coherent antistokes Raman scattering microscopy and UV/vis spectroscopy (Petersen & Henry, 2011). Although spatial resolution is an issue, some have used Fourier transformed infra-red imaging to detect CNTs; however, this is dependent upon unique spectra (Lawrence & Hitchcock, 2011). The unique signatures of CNTs allow the user to visualize them using Raman microscopy (Rao *et al.*, 1997; Wild & Jones, 2007; de la Zerda & Gambhir, 2007). Wild & Jones (2009) demonstrated that two-photon confocal laser microscopy could be used to detect and visualize nanomaterials. They reported that by using two-photon excitation at 690–720 nm in the near infrared they could detect particles and aggregates of CNTs (MWCNT, SWCNT) as well as metals [titanium oxide (TiO_2) and Cerium dioxide (CeO_2)]. However, they were limited to the size range ~70–200 nm (Wild & Jones, 2009). Cherukuri *et al.* (2004, 2006) were also able to visualize SWCNT in cells using near-infrared fluorescence microscopy. Near infrared has also allowed the visualization of MWCNT in other biological systems (Kam *et al.*, 2005). Chae *et al.* (2010) evaluated Fourier transform infrared spectroscopy, SEM with energy-dispersive X-ray spectroscopy, carbon-13 NMR and high-performance liquid chromatography for detection of C60 fullerene. They concluded that only an extractive approach coupled to high-performance liquid chromatography could effectively detect and quantify fullerenes (Chae *et al.*, 2010). The ability to functionalize CNTs provides an opportunity to use nanotags or fluorescent markers conjugated to the nanotube and monitored by CLSM or two-photon laser microscopy. For example,

Table 1. Sources and properties of nanomaterials.

Material	Purity (%)	APS (nm)	SSA (m^2 g^{-1})	Coating	CAS#
CuO	99.8	30	24	none	7440-50-8
TiO_2 anatase-hydrophilic	98	50	28	none	
TiO_2 rutile	99	50	25	none	13463-67-7
TiO_2 hydrophilic	99	50	25	SiO_2	13463-67-7
TiO_2 hydrophobic	99	50	25	Al/Fatty acid	13463-67-7
TiO_2 lipophilic	99	20	25	Al/Silica/Stearic acid	13463-67-7
Ni	99	90	5	None	
CeO_2**	99	<25	50	None	1306-38-3
ZnO	99.9	50	19	Stearic acid	

CNM*	Purity (%)	Dimensions	SSA (m^2 g^{-1})	BD	TD
MWCNT (none)	>95	OD > 50 nm/ID 5–15 nm/lgth10–20 μm	>40	0.05 g cm^{-3}	2.1 g cm^{-3}
SWCNT	>90	OD 1–2 nm/lgth 5–30 μm		(308068-56-6)	
SWCNTOH	>90	OD 1–2 nm/lgth 5–30 μm		(308068-56-6)	
SWCNTCOOH (308068-56-6)	>90	OD 1–2 nm/lgth 5–30 μm			
Fullerene C60 (none)					

Source: *M K Impex Canada (MKnano)
**Sigma-Aldrich, St. Louis, MI, U.S.A.
Abbreviations:
APS, average particle size; SSA, specific surface area; Al, Alumina; CNM, Carbon Nanomaterials; BD, bulk density; TD, true density
(CAS #) = Chemical Abstract Services #

Shi *et al.* (2007) used quantum dots to label nanotubes and imaged them using ultraviolet confocal laser scanning microscopy, although as noted, fluorescent tags may have impacted the behaviour of the material in question. STXM has been used effectively to image and characterize CNTs, particularly in parallel with TEM imaging (Najafi *et al.*, 2010).

Interface of CNTs and aquatic environments. CNTs are extremely reactive materials that are known to be highly sorptive to natural organic matter, extracellular polymeric substances (EPS) and other biomacromolecules (Kang *et al.*, 2009). Proteins, polysaccharides, peptidoglycans, lipids, humics/fluvic acids and products of decomposition should be considered as possible contributors to the coating or corona on CNTs (Lowry *et al.*, 2012). Several reports indicate that the fine-scale coatings that develop on nanomaterials are a significant factor in reducing their toxicity (Lowry *et al.*, 2012). It has been suggested by some authors that CNT interactions with natural organic materials and EPS might make the 'as manufactured' surface chemistry insignificant in fate and toxicity (Petersen *et al.* (2011). Characterization of the coating/corona has been carried out using a range of techniques including extraction (Lynch & Dawson, 2008). To date, most studies have concentrated on defined exposures using commercially acquired natural organic materials or EPS from pure cultures (Quigg *et al.*, 2013). Thus, there is a need for studies addressing questions involving environmental media. Lawrence *et al.* (2014) have applied STXM to examine the complex corona forming on MWCNTs and SWCNTs exposed to river biofilm development. An example of mapping MWCNTs in riverine microbial biofilms is shown in Figure 2(A) whereas 2(B) demonstrates mapping C_{60} fullerene in a biofilm. Each of these three-colour maps is a composite of component maps derived from fitting a C 1s stack to suitable reference spectra. The carbon nanomaterials are in red, the protein is in green whereas polysaccharide (Fig. 2A) or lipid (Fig. 2B) is in blue. The protein and polysaccharides are clearly seen in conjunction with the MWCNT whereas the C_{60} fullerenes are only found in association with protein. STXM allows high-resolution imaging of carbon nanomaterials with sensitive chemical detection of the material and associated biogenerated coatings. As shown by Lawrence *et al.* (2014), these coatings reduce reactive oxygen species production and toxicity of the CNTs. C 1s spectra of C_{60} fullerene, arc discharge MWCNT (Najafi *et al.*, 2008) and chirally specific metallic and semiconducting SWCNT (Rossouw, 2014) are presented in Figure 2(C) indicating the ability to differentiate different carbon nanomaterials, in addition to adhering biomolecules (Lawrence *et al.*, 2014) or covalently linked ligands (Najafi *et al.*, 2010).

Metal and metal oxide NPs (Ce, TiO_2 and Cu)

Metal oxide NPs released into aquatic environments can undergo a number of transformations, such as dissolution,

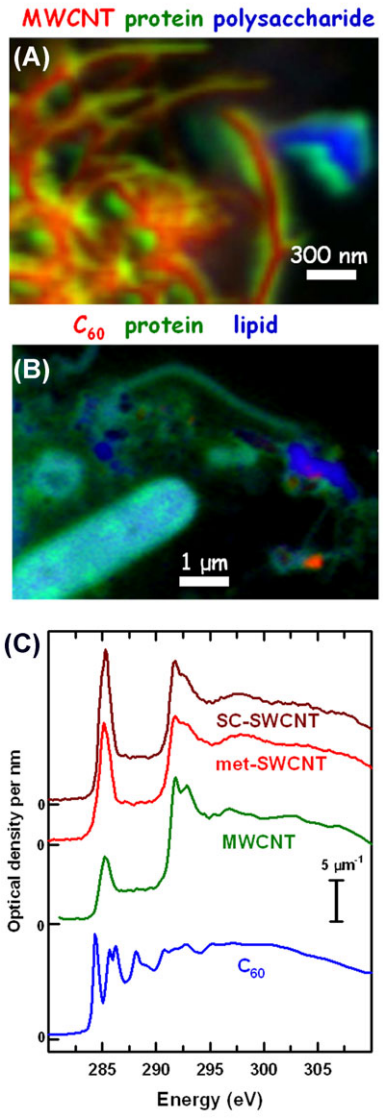

Fig. 2. (A) Three colour composite of component maps of MWCNT (red), protein (green) and polysaccharides (blue) in a microbial biofilm exposed to MWCNT, derived from a C 1s stack (Lawrence *et al.*, 2014). (B) Three colour composite map of C_{60} fullerene (red), protein (green) and lipid (blue) in a microbial biofilm exposed to C_{60}, derived from a C 1s stack (Lawrence *et al.*, 2014). (C) C 1s spectra on an absolute intensity scale of C_{60} fullerene, MWCNT, and metallic and semiconducting SWCNT. The MWCNT spectrum (*Najafi et al.*, 2008) is that without orientation sensitivity, as would be recorded with circular polarization. The SWCNT spectra are actually electron energy loss spectra recorded from individual SWCNT in a TEM, and are presented here due to complications in the corresponding STXM data due to adherent surfactant (see Rossouw *et al.*, 2012).

aggregation, oxidation and reduction. Studies have shown that NPs sorbed by bacterial cells generally induce more toxic effects, acting as a local point source or through direct physical interactions (Li *et al.*, 2012). CeO_2, zinc oxide, cupric oxide (CuO) and TiO_2 NPs are commonly used by industry (Kasemets *et al.*, 2009; Gomes *et al.*, 2013). The following examples demonstrate how STXM at metal 2p, metal 3d and C 1s absorption edges may be used to monitor the interaction of the NP with river biofilms.

CeO_2. CeO_2 NPs are produced industrially for use as a diesel fuel additive (typically at a concentration of 5 mg L^{-1}) and as a polishing agent (Park *et al.*, 2008). Thus, cerium is entering the environment on a relatively large scale due to industrial production and applications in fuels. To assess the fate of CeO_2 NPs, river biofilms were exposed to 1 mg L^{-1} CeO_2 NPs (<25 nm) for 3 days. The interaction of the biofilms with the CeO_2 NPs was examined by collecting image sequences (stacks) at specific energies across the Ce 3d edge and the C 1s edges over the same area. A 50-nm pixel size was used. Smythe *et al.* (2013) showed that Ce oxidation states (III, IV) could be differentiated using the Ce 3d edge and Kaindl *et al.* (1984) showed that ligands also influenced the spectra. Principle component analysis showed that only CeO_2 NPs were present in the biofilm; that is, there were no obvious transformations (e.g. dissolution, reduction) of the CeO_2 NP in the biofilm. Subsequently, CeO_2 NPs in the biofilm were mapped by fitting the Ce stack to a linear combination of the quantitative (d = 7.65 g cm^{-3}) CeO_2 3d spectrum and a slowly varying featureless signal (Dynes *et al.*, 2006a, b). The derived CeO_2 component map is shown in Figure 3(F). The CeO_2 NPs apparently formed aggregates which likely contributed to lower reactivity and limited dissolution. Aggregation of CeO_2 nanomaterials appears common (Shah *et al.*, 2012) and aggregates up to 400 nm have been reported (Van Hoecke *et al.*, 2009). The maximum thickness of the CeO_2 NP aggregates was 30 nm, and the average thickness was 5 nm (NB: this value incorporates non-CeO_2 materials and empty space). The speciation of Ce in soybean plants grown in soil spiked with CeO_2 NPs was examined using XRF at the Ce 2p edge (Hernandez-Viezcas *et al.*, 2013). Similar to these observations, the Ce species in plant tissues was mainly that of the original CeO_2 NPs [i.e. Ce(IV)], although a small percentage had been biotransformed to Ce(III). Nanoceria are often viewed as oxygen buffers with redox cycling between the Ce(III) and the Ce(IV) oxidation states allowing them to act as free radical scavengers. However, it appears that this quality may contribute to both the toxicity and potential protective qualities of nanoceria, depending upon the specific environment. Thus, there are some reports where no detectible effects on bacteria were detected, and others where significant impacts have been observed (Van Hoecke *et al.*, 2009). These authors predicted that the no-effects concentration for aquatic habitats would be between 0.052 and 0.108 mg L^{-1}. However, they did not observe the strong sorption of nanoceria to cell surfaces reported by Thill *et al.* (2006), which appears to be an important aspect of toxicity.

>The C 1s stack (which also includes the K 2p edge) from the CeO_2 exposed biofilm was fit to a linear combination

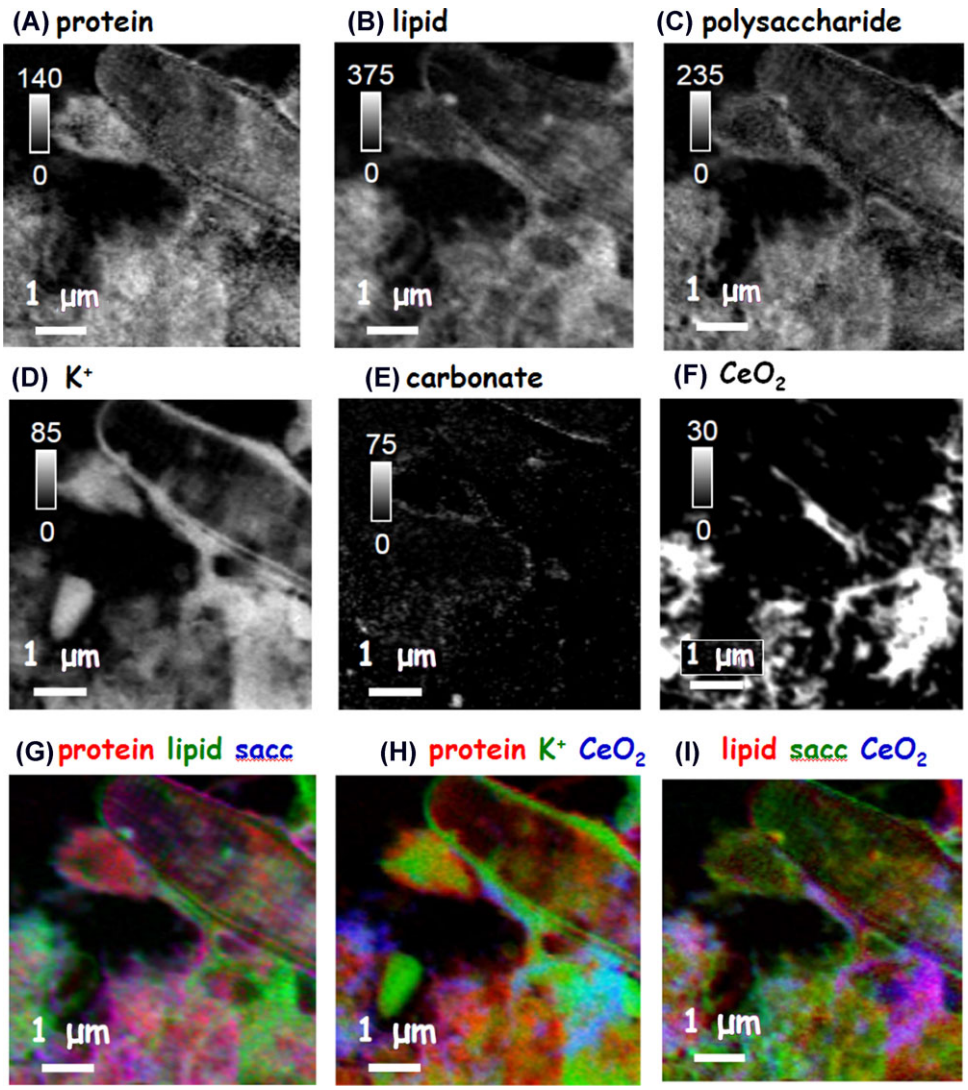

Fig. 3. Component maps of river biofilms exposed to 1 mg CeO_2 mL^{-1} for 3 days. (A) protein, (B) lipid, (C) polysaccharide, (D) K^+, (E) carbonate and (F) CeO_2. Maps (A–E) were derived by linear combination spectral fitting of a C 1s image sequence (280–320 eV) using singular value decomposition (SVD). The CeO_2 map was derived by linear combination spectral fitting of a Ce 3d edge image sequence (870–915 eV). The grey scale indicates thickness in nanometers. Selected colour overlays of the component maps. (G) red = protein, green = lipid, blue = polysaccharide. (H) red = protein, green = K, blue = CeO_2. (I) red = lipid, green = polysaccharide, blue = CeO_2.

of six quantitative reference spectra, representative of proteins (albumin), lipids (1,2-Dioleoyl-sn-glycero-3-Phosphatidylcholine), polysaccharides (xanthan gum), carbonates (aragonite), K and a slowly declining, featureless signal (silicate), the spectra of all of which have been reported previously (Dynes et al., 2006b). The component maps from the fitting are shown in Figure 3, as well as RGB composites of the biomolecules component maps (Fig. 3G) and selected biomolecules with the CeO_2 component map (Figs. 3H and I). The biofilm was found to be rich in protein, lipid and polysaccharides. The region examined included a diatom, in addition to several types of bacteria and extracellular materials. The CeO_2 NPs were mainly associated with lipids (compare Figs. 3B and F). CeO_2 NPs were also associated with the diatom frustule surface, both on the edge and the middle of the diatom, although the amount was less than that observed in other areas of the biofilm. The observed distribution of nanoceria in our studies and the lack of chemical transformation of the CeO_2 appears consistent with the conclusions of Van Hoecke *et al.* (2009) that direct contact is responsible for toxicity of nanoceria to bacteria and algae, rather than uptake or adsorption of NPs, ionic cerium or indirect effects such as shading.

TiO_2. Titanium dioxide is a very effective photocatalyst and finds applications as NPs and nanocoatings for water and air purification and for self-cleaning surfaces. Its strong oxidation

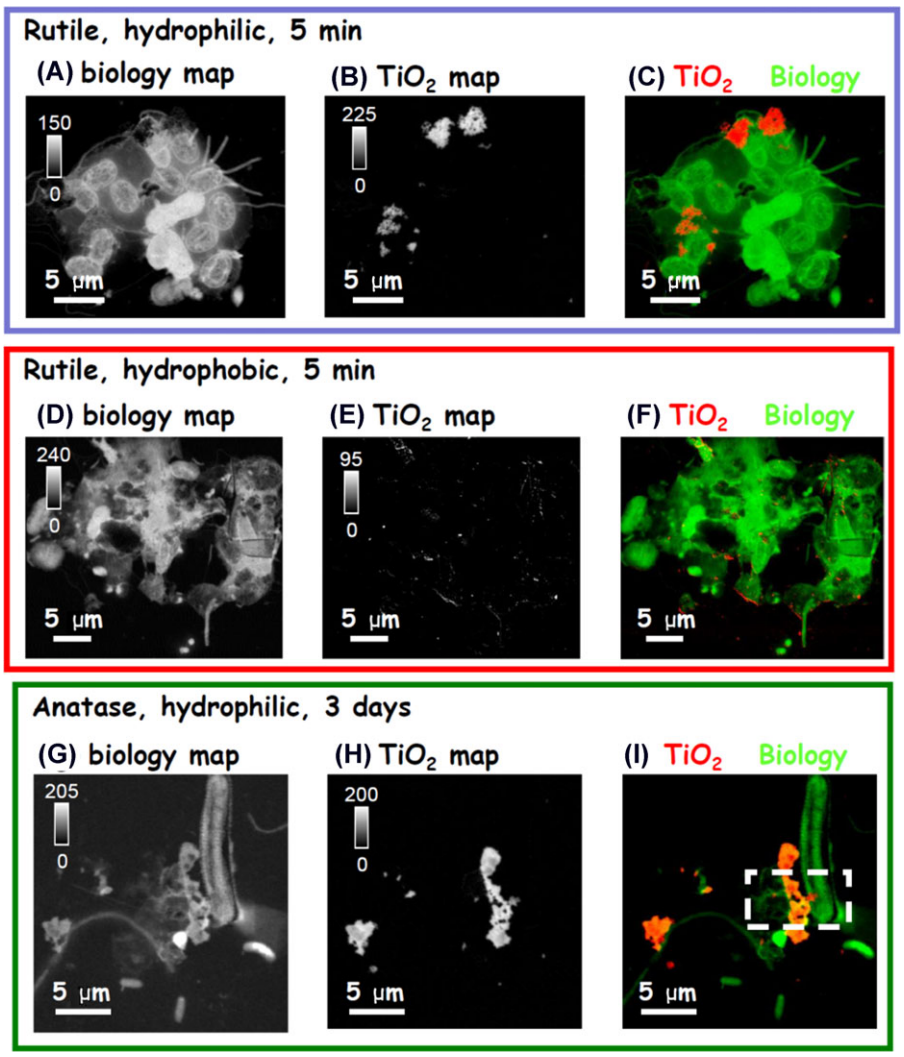

Fig. 4. (A, D, G) Biology ($OD_{288.2eV} - OD_{280eV}$) and (B, E, H) Ti ($OD_{460eV} - OD_{452eV}$) image difference maps, and (C, F, I) their colour overlays (TiO_2 = red, and biology = green), of biofilms exposed to (upper) hydrophobic rutile for 5 min, (middle) hydrophilic rutile for 5 min and (lower) to hydrophilic anatase for 3 days. The grey scale indicates effective thickness in nanometers. The white rectangle in the anatase colour overlay (I) indicates the area from which a full Ti 2p image sequence was acquired.

activity and superhydrophilicity also makes it a very effective antibacterial agent. Thus, it is not surprising that even in 2008, Mueller & Nowack (2008) estimated that up to 47 300 kg $year^{-1}$ of TiO_2 might enter surface waters in Switzerland alone. These environmental loadings give rise to concerns regarding their fate and activity in freshwaters. Experiments were performed in which river biofilms were exposed to 1 mg mL^{-1} hydrophobic or hydrophilic rutile (TiO_2) NPs (<50 nm) for 5 m. STXM difference maps (on/off characteristic energies) at the C 1*s* and Ti 2*p* edges were acquired of the TiO_2-exposed biofilms as shown in Figures 4(A–C) and (D–F). The C 1s difference map $OD_{288\,eV} - OD_{282\,eV}$ predominantly shows the biological entities (bacteria, algae, cyanobacteria) since protein absorbs at 288.2 eV. In the hydrophilic rutile system, aggregates of TiO_2 NPs appeared to be mainly associated with the EPS of the bacterial colony (likely cyanobacteria based on their size). Similarly, in the hydrophobic rutile system, aggregates of TiO_2 NPs were associated with the EPS or outer surfaces of the biological entities (e.g. flagellates). Auroja *et al.* (2009) showed that algae can be entrapped by TiO_2 aggregates. The hydrophobic rutile NPs appear to be smaller than the hydrophilic rutile NPs.

River biofilms were also exposed to 1 mg mL^{-1} hydrophilic anatase (TiO_2) NPs (<50 nm) for 3 days. The C 1s and Ti 2p difference maps (50-nm pixel size) of the anatase exposed biofilms are shown in Figures 4(G–I). Similar to the rutile exposed biofilm the TiO_2 formed aggregates and was associated with the biofilm. The area outlined in a dashed white rectangle in Figure 4(I) was examined in more detail to look at the speciation of the TiO_2 by collecting a full Ti 2*p* stack

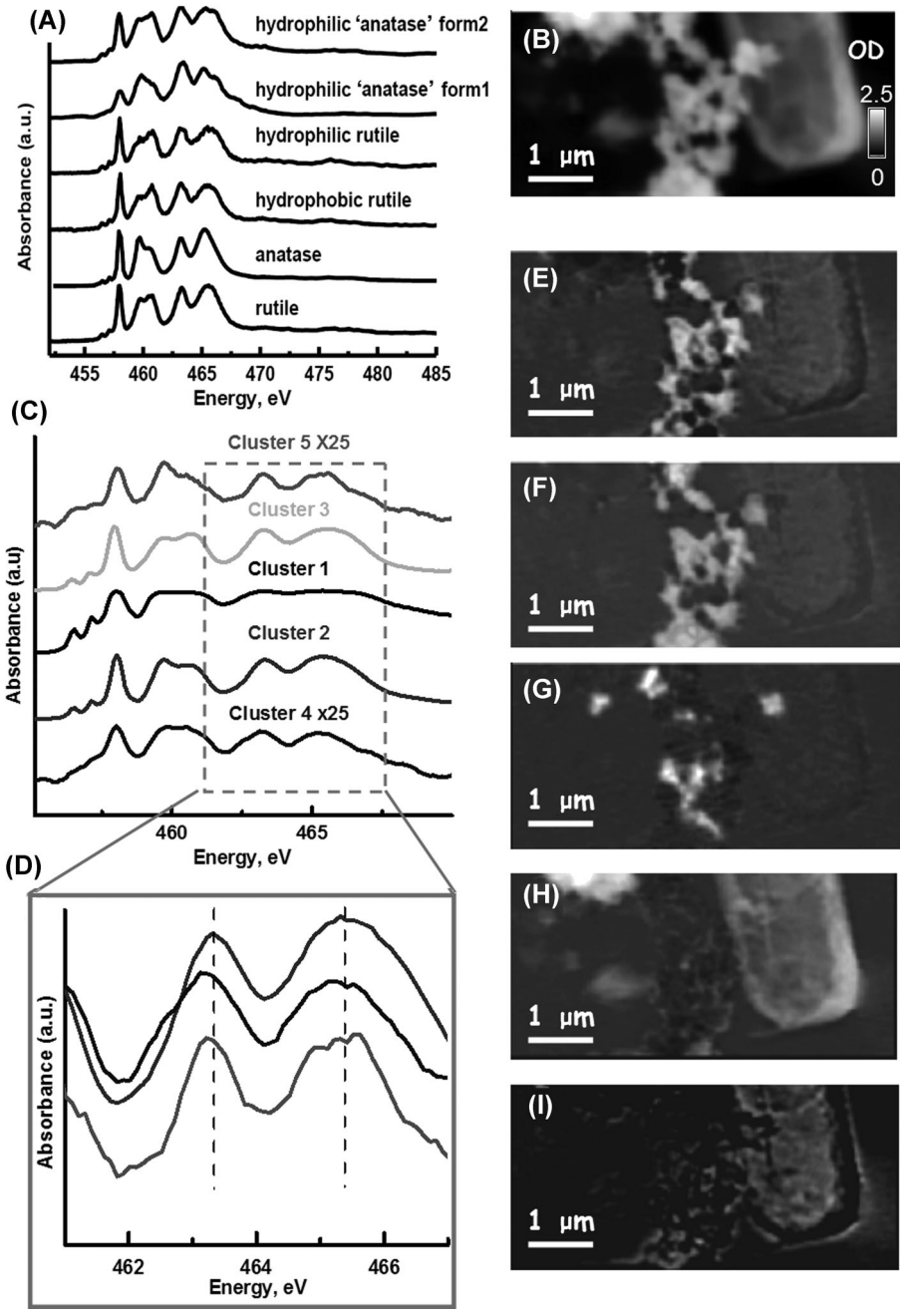

Fig. 5. Ti 2p analysis of the biofilm exposed to hydrophilic anatase for 3 days. (B) Ti 2p reference spectra of rutile and anatase compared to the spectra from the commercial hydrophilic anatase. The hydrophilic anatase was actually a mixture of rutile and anatase. (B) Average image of the Ti 2p stack. Principal component and cluster analysis of the Ti 2p stack. (C) Derived cluster spectra. (D) Enlargement of the peaks in the $2p_{1/2}$ region for the cluster 2, 3 and 4 spectra, showing a shift to lower energy for TiO_2 sorbed by the biofilm (cluster 4, Fig. 5H) compared to that of the unsorbed TiO_2 nanoparticles (NP) (clusters 2 and 3), indicating that there was a chemical interaction between the biofilm and the NP. (E–H) Component maps of clusters 1–5.

(50-nm pixel size). These results are presented in Figure 5. The Ti 2p spectrum is sensitive to the Ti oxidation state, coordination environment and second coordination sphere (Henderson *et al.*, 2002). The Ti 2p spectrum obtained from the commercial hydrophilic anatase showed that it was actually a mixture of anatase and rutile (see Fig5.A). The nature of the hydrophilic properties in the hydrophilic anatase was not identified by the supplier (see Table 1) but it probably arises from coatings (e.g. SiO_2, Al_2O_3) (Bolis *et al.*, 2012). The Ti 2p spectra indicate that the coating on the anatase/rutile had not changed the structure of the TiO_2. The Ti 2p stack was analysed using a principle component analysis followed by a cluster analysis

using a Euclidian metric (Lerotic *et al.*, 2004). This showed that there were potentially five differentiable Ti species present in the biofilm (Fig. 5C). The first, second and third cluster components are signals from the TiO_2 NPs. The cluster spectra (Fig. 5C) are very similar, as are the associated cluster images (maps of the distribution of the cluster component) for clusters 1 and 2 (Figs. 5E and F). Cluster 3 is attributed to zones of 'pure' anatase (Fig. 5G) whereas cluster 2 is attributed to rutile (F) and cluster 1 is from pixels where the Ti 2p spectrum is distorted by absorption saturation (E). The fourth (Fig. 5H) and fifth (Fig. 5I) cluster components are TiO_2 sorbed to components of the biofilm. This sorbed TiO_2 was not apparent from the image difference map, presumably due to its low concentration (OD ~0.02–0.05) and the high background on which they occurred. The poor signal/noise ratio in the fourth cluster spectrum makes it impossible to see whether the speciation of the sorbed Ti had changed. In their study of the reaction of TiO_2 with CNTs, Zhang *et al.* (2012) showed that the Ti 2p peaks shifted to lower values, implying that there was a chemical interaction between the TiO_2 and carbon in the nanotubes. This interaction is due to electron transfer from titania to the nearby carbon layer, which facilitates the Ti 2p → 3d transition. Furthermore, they observed the formation of a new peak which indicated a change from the octahedral coordination of Ti, likely forming a five-coordinated structure. Figure 5(D) compares the Ti 2p spectra of the TiO_2 NPs (clusters 1, 2 and 3) and the TiO_2 sorbed to the biofilm (clusters 4 and 5). This shows that the peaks in the spectrum of the sorbed TiO_2 are shifted 0.1–0.2 eV lower relative to the TiO_2 NP spectrum, indicating the TiO_2 NPs were interacting chemically with the biofilm. SEM images of algae (*Pseudokirchneriella subcapitata*) exposed to TiO_2 NPs showed that algal cells can adsorb about 2.3 times their own weight in TiO_2 particles on the surface (Huang *et al.*, 2005). The Ti 1s edge has been used for Ti speciation in cucumbers which had accumulated Ti when grown on soil amended with TiO_2 NPs (anatase and rutile) (Servin *et al.*, 2013). The translocation of TiO_2 NPs from the root to the cucumbers was shown to occur without biotransformation. Oxidative stress mediated by photoactive TiO_2 is the most frequently cited mechanism for toxicity (Battin *et al.*, 2009; Miller *et al.*, 2012) and involves the close association of NPs with the cell surface where reactive oxygen species and damage to the cell envelope occurs. In our systems, there does not appear extensive transformation, dissolution or redistribution of the Ti. Although most experimentation has occurred at levels of Ti far exceeding the predicted environmental concentrations (0.016 mg L^{-1} for TiO_2), Battin *et al.* (2009) were able to show effects at low concentrations in complex aquatic microbial communities.

CuO. Copper containing NPs have a relatively extensive range of applications, including catalysts, wood preservatives and antimicrobials, notably in fabrics (Cox 1991; Zhou *et al.*, 2006; Ren *et al.*, 2009). They can enter the aquatic environment by a number of means, but principally via run off and municipal waste-water effluents. In this study, the Cu 2p and the C 1s spectra were used to examine a river biofilm exposed to CuO NPs for 5 m. Figure 6(A) shows an overlay of the Cu(II) image difference map ($OD_{931.3} - OD_{928eV}$) and the biology image difference map ($OD_{288.2} - OD_{280eV}$). This shows that the CuO NPs were aggregated and that they were associated with the biofilm. To examine the Cu speciation in the biofilm, a Cu 2p stack was collected from a smaller area. Spectral fitting of the stack with the Cu 2p spectrum of the CuO NP (Fig. 6B) showed that, in addition to the CuO NP aggregates associated with the biofilm, CuO was also found at the edges of a diatom (see Figs. 6C–E). The Cu(II) peak in the Cu 2p spectrum obtained by threshold masking the signal at the edge of the diatom was found to be about 0.4 eV lower than the corresponding signal from the mass of aggregated CuO NP (see Fig. 6B). This was attributed to chemical transformation in the sorption of CuO. A similar result was reported by Lawrence *et al.* (2012). Given the environmental conditions present in South Saskatchewan River water, in particular, low dissolved organic carbon and relatively high electrolytes, aggregation of CuO NPs is expected (Gao *et al.*, 2009). The other critical factor in the fate of CuO NPs was the observation of apparent dissolution or the existence of the mobile ionic phase which could sorb to EPS and cells surfaces. This redistributed the CuO within the biofilm community, an aspect of toxicity and fate not observed for the more stable TiO_2 and CeO_2 NPs discussed above.

Probing detection limits – XRF yield versus transmission detection

Nickel occurs in aqueous environments as a result of natural sources such as acid rock drainage or from mining and smelting activities. Microorganisms are known to bioaccumulate Ni (Rajendran *et al.*, 2002). Since microorganisms are an important food source for other organisms, particularly in rivers (Lawrence *et al.*, 2002, 2004), there is a concern that the food chain may be impacted in areas exposed to excess levels of Ni. Investigations of Ni in natural aquatic environments may establish how Ni accumulates, and how it moves through the food chain. Eickhoff *et al.* (2014) used STXM to investigate the influence of silica of partitioning of Ni between biogenic and abiogenic ferrihydrite. Dynes *et al.* (2006a) exposed a natural river biofilm to 1 mg L^{-1} Ni^{2+} for 24 h, and examined it with STXM at the O 1s and Fe, Mn and Ni 2p edges. They showed that STXM was effective for quantitative metal mapping in complex biological systems. Furthermore, that work showed that Ni was associated with Mn, and that Mn was associated with biology, perhaps binding to the EPS coating algae or cyanobacteria. Hitchcock *et al.* (2009) then examined a similar natural river biofilm exposed to 10 mg L^{-1} Ni^{2+} for 24 h. The higher Ni concentration addressed a number of issues related to STXM sensitivity encountered at the lower

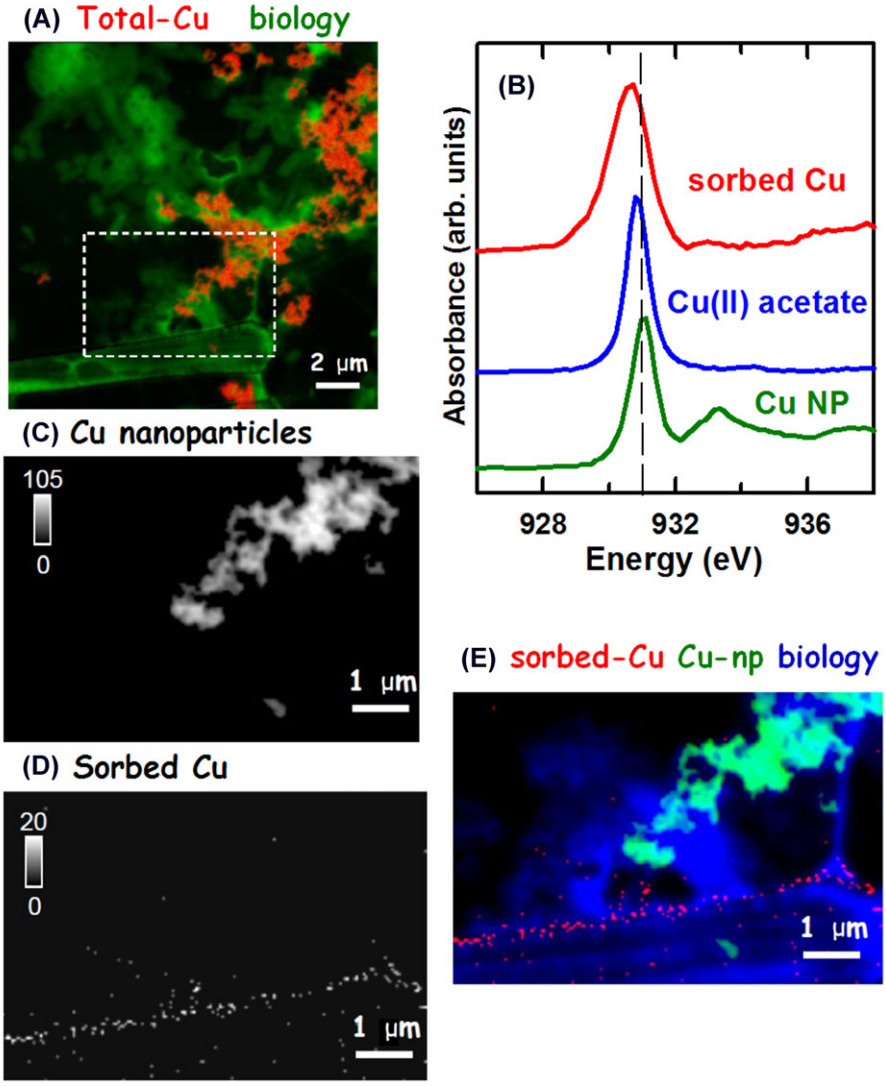

Fig. 6. Analysis of a river biofilm exposed to Cu NP. (A) Colour overlay of image difference maps (red = total Cu, green = biology). The white rectangle indicates the area from which a full Cu 2p stack was recorded. (B) Cu $2p_{3/2}$ spectra of Cu nanoparticles (NP) and Cu sorbed by the biofilm, compared to that of Cu acetate, a reference Cu(II) compound. Component maps of (C) Cu NP, and (D) sorbed Cu were derived from the Cu 2p stack by linear combination spectral fitting using the Cu NP and the sorbed Cu spectra, converted to an absolute response scale (OD nm^{-1}) The grey scale is thickness in nm. (E) Colour composite of component maps for the biology (no Cu 2p signal) – blue, Cu NP – green and sorbed Cu – red.

Ni concentration. The 1 mg L^{-1} Ni^{2+} resulted in Ni levels in the biofilm that were just above the detection limit for transmission detection using our acquisition conditions. A longer dwell time could have been used to increase the sensitivity, but radiation damage would have increased and metal species are known to be reduced through X-ray damage. Here, we report a study of a similar Ni-exposed natural river biofilm, but in this case we have used much more sensitive XRF detection as well as transmission detection to explore the detection limits and to study several regions of a natural river biofilm exposed to either 1 or 10 mg L^{-1} Ni^{2+} for 24 h prior to harvesting and preparation for STXM measurements.

Figure 7(A) presents an O 1s image recorded at 540 eV whereas (B) is the same image with superimposed colour-coded maps of biological (green), Fe (red) and Ni (blue) signals derived from STXM measurements on the 10 mg L^{-1} Ni^{2+} exposed sample using transmission detection. Large-scale images (not shown) indicate fewer microorganisms in the sample and a shift from a population dominated by green algae to one dominated by diatoms with silica-rich frustules, when comparing the 1 and 10 mg L^{-1} Ni^{2+} samples, consistent with increased toxicity at higher Ni^{2+} concentrations. Figures 7(C) and (D) are the Ni map and a colour composite image from Ni 2p transmission measurements on the 1 mg L^{-1} Ni^{2+}-exposed

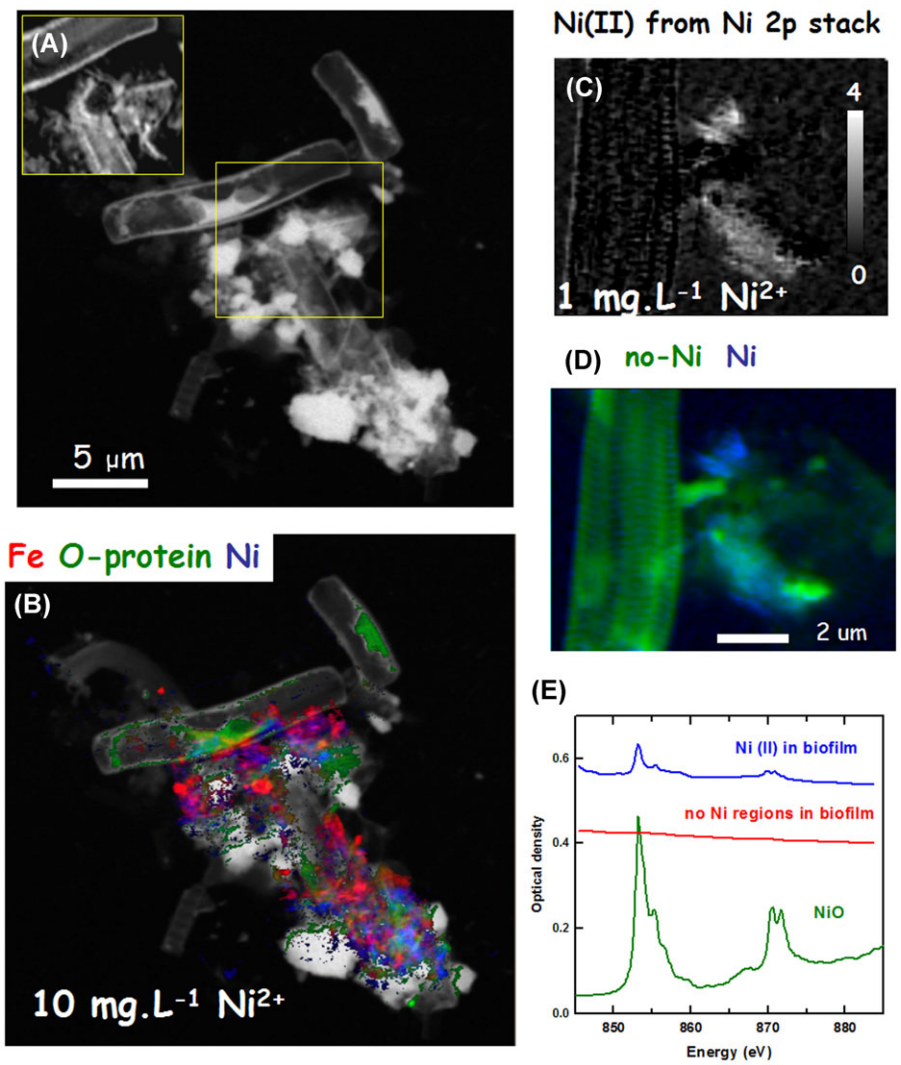

Fig. 7. (A) X-ray absorption image (532.1 eV, 400 × 400 pixels, 1 ms pixel^{-1}) of a Ni biofilm exposed for 24 h to 10 mg L^{-1} Ni^{2+}. The inset image in the upper left is the same area as in the middle rectangle, but imaged at 520 eV, below the O 1s edge. (B) Composite of three species-specific component maps derived from difference of two X-ray images (400 × 400 pixels, 1 ms pixel^{-1}) recorded in transmission and converted to OD: Fe(III) (red) – OD_{710} – OD_{704}; protein (green) from O 1s – OD_{532} – OD_{528}; Ni(II) (blue) – $OD_{852.5}$ – OD_{850}. The intensity is rescaled within each colour. The coloured composite is superimposed on the image recorded at 532.1 eV. (C) Ni map in a region of a river biofilm exposed for 24 h to 1 mg L^{-1} Ni^{2+}. The grey scale indicates thickness in nm. (D) Colour-coded composite of component maps for no-Ni and Ni derived from the Ni 2p stack. (E) Spectrum of Ni-rich regions extracted from the Ni 2p stack, compared to spectra of NiO (pure) and the stack spectrum of regions found not to contain Ni.

sample. Figure 7(E) compares the Ni 2p spectrum extracted from the pixels where Ni was detected. Although the signal was detectable and showed the Ni was still in the Ni(II) oxidation state, the signal quality was very poor.

When XRF rather than transmission detection was used, a much clearer result for Ni detection was obtained. Figure 8(A) plots XRF spectra extracted from a (10 μm × 8.5 μm, 46 × 40 pixel, 120 ms) XRF map recorded using 854 eV incident photon energy from an area of the river biofilm exposed to 10 mg L^{-1} Ni^{2+} for 24 h. Peaks from Ni, Fe, O, N and C were detected, whereas that from Mn was not resolved from the large O K_α signal. Figure 8(B) plots Ni 2p absorption spectra from three spatial regions recorded with XRF-yield detection over the Ni L_3 edge. The locations where the spectra were obtained are indicated in the inset images in Figure 8(B). The spectrum in most of the diatom (red) showed little or no Ni 2p structure – the residual signal corresponded to a combination of XRF detector background and elastic scattering. The spectrum of dispersed zones off the diatom, as well as one on the diatom (blue), exhibited a strong Ni 2p spectrum which was Ni in the Ni(II) oxidation state, based on the similarity to the Ni 2p spectrum of NiO (Dynes *et al.*, 2006a; Hitchcock *et al.*,

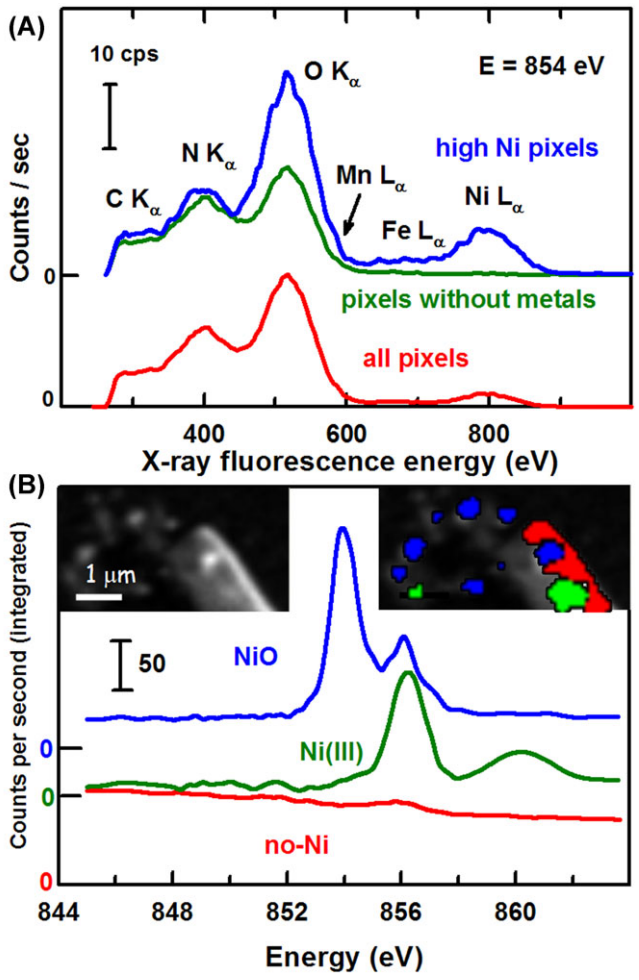

Fig. 8. (A) X-ray fluorescence (XRF) spectra measured with photon energy at the Ni(II) $2p_{3/2}$ peak (854 eV) derived from an X-ray fluorescence map (XRF spectrum at each pixel). The spectrum of all pixels (red), the spectrum of all regions without any metal XRF signal (Ni, Fe) (green), and the spectrum with high levels of Ni Lα signal (blue) are plotted. The blue and green curves are offset for clarity and the zero for that signal is indicated. (B) X-ray absorption spectra measured using the signal integrated over the Ni Lα XRF peak (760–840 eV) (XRF-yield XAS), extracted from an XRF-XAS stack over the Ni $2p_{3/2}$ edge in regions without Ni (red), selected pixels where the Ni oxidation state is Ni(II) (based on match to the spectrum of NiO) (blue) and a region in the diatom where there is a large chemical shift of the Ni $2p_{3/2}$ peaks indicating a higher oxidation state, most likely Ni(III) (green). The blue and green curves are offset for clarity; the zeros for all three signals are indicated. The image inserted at upper left is the average of all images in the Ni Lα yield stack. The coloured regions image in the upper right image indicate the pixels selected to generate the XRF-yield XAS spectra.

2009). Interestingly, a third Ni 2p spectral signature (green) was found in a specific region of the diatom. At this location, the two characteristic structures typical of Ni 2p spectra (corresponding approximately to the t_{2g} and e_g components of an octahedral crystal field) were observed but they were shifted about 2.2 eV higher in energy relative to the corresponding features in NiO. This chemical shift indicates a higher oxidation state, most likely Ni(III) as the shift in peak position is similar to that reported in the literature for Ni(III) compounds (Wang *et al.*, 2000, 2001; Gu *et al.*, 2014). The XRF-yield X-ray absorption spectrum in the Ni containing regions is of high quality and has very low background, indicating excellent rejection of elastic scattering. This is critical since the elastic scattering signal in the 840–860 eV region overlaps the Ni Lα XRF signal (849 eV).

Figure 9 compares component maps derived from the XRF-XAS stack (XRF spectra recorded at each pixel and at each incident photon energy in the mapped region) from XRF and the transmission signal recorded simultaneously from the same area of the 10 mg L^{-1} Ni^{2+} river biofilm sample from which the XRF and XRF-yield-XAS spectra shown in Figure 8 were obtained. The distribution of the regions without Ni ('no-Ni') and the dispersed Ni(II) was similar in both detection channels, but the XRF-XAS signal was of higher statistical quality (despite being constructed from orders of magnitude fewer detected photons) and there were artefacts at the edges of the diatom frustule in the Ni(II) map derived from the transmission data. The Ni(III) signal was only detected in the XRF-XAS signal. Although there was apparent structure in the Ni(III) map derived from fitting the transmission Ni 2p stack data, all of that structure was artifactual since the X-ray absorption spectrum extracted from the strong features in that map did not exhibit any detectible Ni 2p signal. Figure 10 compares the Ni 2p spectra from the no-Ni, Ni(II) and Ni(III) regions measured simultaneously in transmission (A) and XRF-yield (B). Although a weak Ni 2p signal from the Ni(II) regions was detected, there was no evidence of the Ni(III) spectral signal in the transmission-based absorption spectrum extracted from the region identified as Ni(III) from the unambiguous XRF signal.

This data set, which shows Ni 2p signals for both transmission and XRF-yield, provides a means to estimate the amount of Ni being detected in these Ni-rich regions. A detailed analysis will be presented elsewhere. Note that as the concentrations of interest get lower, the advantage of XRF mapping and XRF-yield absorption spectromicroscopy get larger, as was found in a recent study of arsenic immobilization by an Fe(II)-oxidizing freshwater bacteria (Hitchcock *et al.*, 2012).

Correlative microscopy applications involving STXM

In general terms, correlative microscopy is where more than one method is used to study the same region or features in a sample. As noted above and by Hitchcock (2012), STXM is most powerful when it is part of a correlative suite of techniques applied to a particular problem, ideally with measurements on the same area of the same sample, as reported for the combination of CLSM, TEM and STXM by Lawrence *et al.* (2003). Neu *et al.* (2010) similarly noted the value of correlative

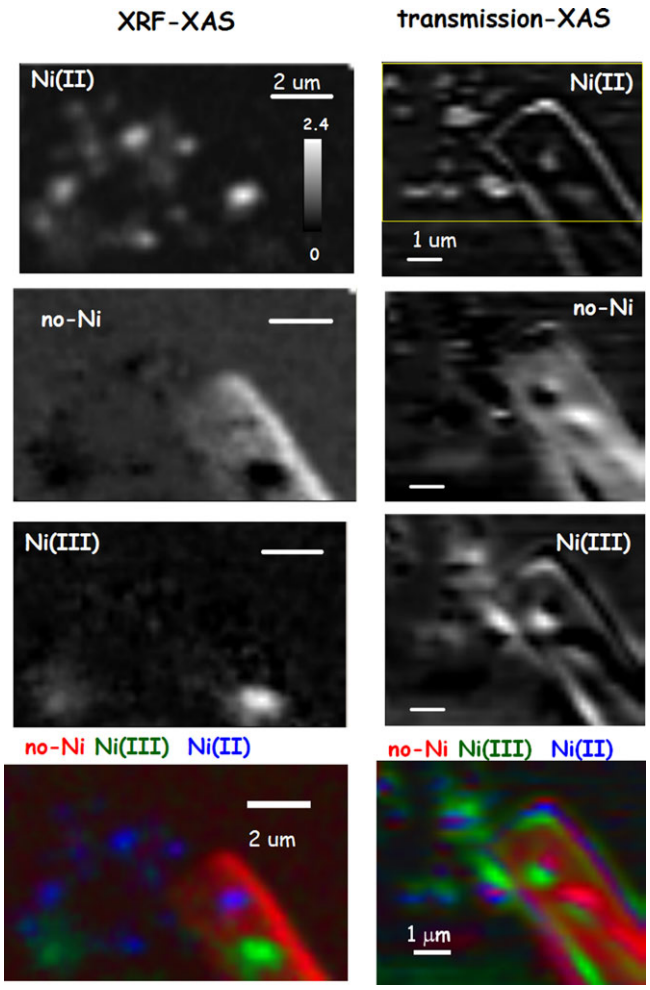

Fig. 9. Comparison of Ni detection and speciation by X-ray fluorescence (left) versus transmission (right). In each column, there are component maps for Ni(II), no-Ni and Ni(III) along with a colour composite. The measurements were not made at the same time for technical reasons and the transmission data covers a larger area that the XRF-XAS (yellow rectangle). Although the Ni(II) signal was detected (weakly, and without accuracy) the second type of Ni, tentatively attributed to Ni(III) was not detected at all in the transmission data – see Fig. 10. The apparent rim of Ni(II) around the diatom frustule is an artefact of residual image misalignment combined with the extremely weak Ni 2p signal in transmission mode. Note that the dwell time per pixel used in these XRF-yield measurements was only 0.12 s.

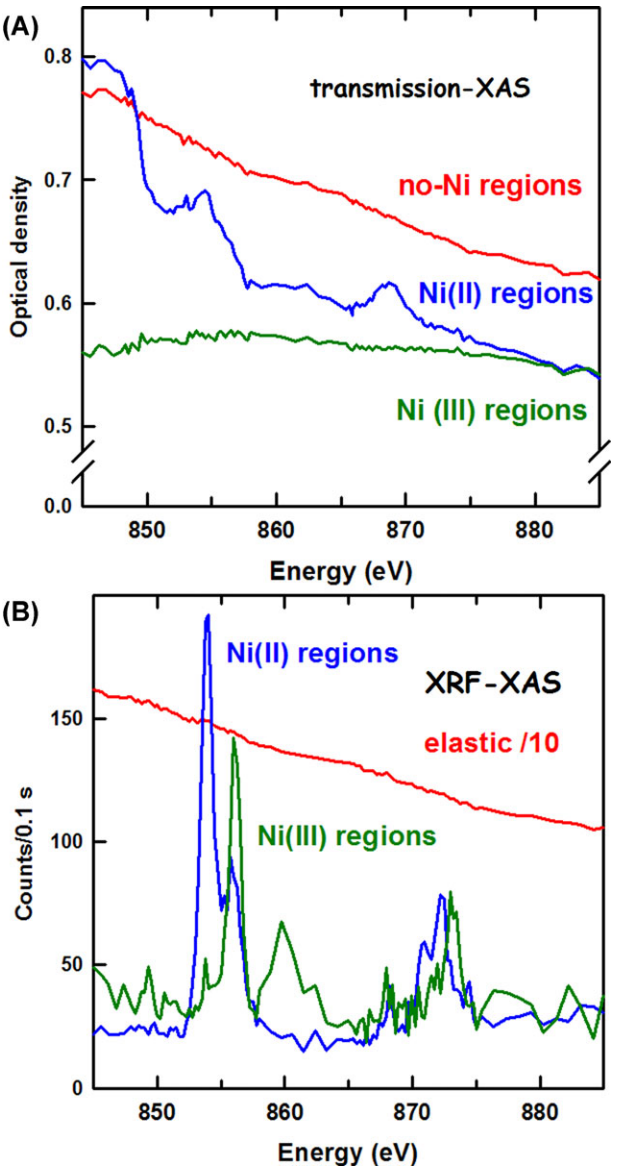

Fig. 10. (A) Transmission XAS spectra of no-Ni regions, Ni(II) regions and the region identified by XRF-XAS as Ni(III). (B) XRF-XAS spectra of the corresponding spatial region. The total fluorescence yield spectrum (red) is compared to the spectra for Ni(II) (blue) and Ni(III), which are taken from the same stack and the same areas as for the transmission signals in (A).

approaches. The most common situation is when light or fluorescence microscopies are applied to an STXM or TEM sample to pre-identify a region of interest and assist in navigation to the location. Increasingly one or more complementary analytical microscopies are used to examine the same region of a sample as studied by STXM in order to provide alternative contrast, higher resolution or complementary chemical information. A number of papers have shown the utility of correlative microscopy methods in general (Caplan *et al.*, 2011; Jahn *et al.*, 2012), and STXM in combination with other approaches, in particular. For example, TEM has been combined with STXM for analysis of the same sample as described in Najafi *et al.* (2010, 2012). Lawrence *et al.* (2003) used an approach where the same location was stained with fluors for CLSM imaging followed by assessment of the same location with STXM. In that case, the fluorescent stains specifically targeted EPS and the STXM imaging confirmed, based on X-ray absorption, that these targets were indeed present at the locations indicated by CLSM.

Conclusions

We have demonstrated through a series of examples, that STXM performed on carbon and metal-based nanomaterials in environmental samples can effectively detect, speciate and quantify these materials in complex biological matrices such as microbial biofilms. In addition, relatively simple sample preparation allows environmentally relevant samples to be examined at high resolution using STXM in either transmission or XRF modes. Speciation was possible for Cu, Ti and Ce oxide nanomaterials using the metal absorption edges whereas the C 1s edge was used to examine both carbon nanomaterials as well as the complex coatings which develop on the surfaces of nanomaterials in the environment. These changes are highly relevant to interpreting the fate and toxicological effects of all types of nanomaterials. The much higher sensitivity and lower detection limits that can be achieved with XRF-STXM was demonstrated with a Ni-biofilm example. Limitations do exist in terms of sample size, thickness and sampling frequency, although these are usually manageable given the high spatial resolution and extensive information provided by STXM.

Acknowledgements

This work was funded through Environment Canada's Chemicals Management Plan and the Natural Sciences and Engineering Research Council of Canada. A.P.H. is supported by a Canada Research Chair. STXM data were acquired at beamline 10ID1 at the CLS. CLS is supported by the Natural Sciences and Engineering Research Council of Canada, the National Research Council Canada, the Canadian Institutes of Health Research, the Province of Saskatchewan, Western Economic Diversification Canada and the University of Saskatchewan. We thank the staff scientists at the CLS (Chithra Karunakaran, Jian Wang) for their support.

References

Aruoja, V., Dubourguier, H.-C., Kasemets, K. & Kahrua, A. (2009) Toxicity of nanoparticles of CuO, ZnO and TiO_2 to microalgae *Pseudokirchneriella subcapitata*. *Sci. Total Environ.* **407**, 1461–1468.

Badireddy, A.R., Wiesner, M.R. & Liu, J. (2012) Detection, characterization, and abundance of engineered nanoparticles in complex waters by hyperspectral imagery with enhanced darkfield microscopy. *Environ. Sci. Technol.* **46**, 10081−10088.

Battin, T.J., Kammer, F.V.D., Weilhartner, A., Ottofuelling, S. & Hofmann, T. (2009) Nanostructured TiO_2: transport behavior and effects on aquatic microbial communities under environmental conditions. *Environ. Sci. Technol.* **43**, 8098–8104.

Bazylinski, D.A. & Frankel, R.B. (2004) Magnetosome formation in prokaryotes. *Nat. Rev. Microbiol.* **2**, 217–230.

Bazylinski, D.A., Lefèvre, C.T. & Schüler, D. (2013) Magnetotactic bacteria. *The Prokaryotes* (ed. by E. Rosenberg, E.F. DeLong, S. Lory, E. Stackebrandt & F. Thompson), pp. 453–494. Springer, Berlin, Heidelberg.

Berciaud, S., Cognet, L., Poulin, P., Weisman, R.B. & Lounis, B. (2007) Absorption spectroscopy of individual single-walled carbon nanotubes. *Nano Lett.*, **7**, 1203–1207.

Bluhm, H., Andersson, K., Araki, T., *et al.* (2006) Soft X-ray microscopy and spectroscopy at the molecular environmental science beamline at the advanced light source. *J. Electron Spectros. Relat. Phenomena* **150**, 86–104.

Bolis, V., Busco, C., Ciarletta, M., Distasi, C., Erriquez, J., Fenoglio, I., Livraghi, S. & Morel, S. (2012) Hydrophilic/hydrophobic features of TiO2 nanoparticles as a function of crystal phase, surface area and coating, in relation to their potential toxicity in peripheral nervous system. *J. Colloid Interface Sci.* **369**, 28–39.

Boxall, A.B.A., Tiede, K. & Chaudhry, Q. (2007) Engineered nanomaterials in soils and water: how do they behave and could they pose a risk to human health? *Nanomedicine* **2**, 919–927.

Caplan, J., Niethammer, M., Taylor, R.M. & Czymmek, K.J. (2011) The power of correlative microscopy: multi-modal, multi-scale, multi-dimensional. *Curr. Opin. Struct. Biol.* **21** 686–693.

Chae, S.-R., Ernest, M.H., Xiao, Y., Rose, J. & Wiesner, M.R. (2010) Comparison of methods for fullerene detection and measurements of reactive oxygen production in cosmetic products. *Environ. Eng. Sci.* **9**, 797–804.

Cherukuri, P., Bachilo, S.M., Litovsky, S.H. & Weisman, B. (2004) Near infrared fluorescence microscopy of single-walled carbon nanotubes in phagocytic cells. *J. Am. Chem. Soc.* **126**, 15638–15639.

Cherukuri, P., Gannon, C.J., Leeuw, T.K., Schmidt, H.K., Smalley, R.E., Curley, S.A. & Weisman, R.B. (2006) Mammalian pharmacokinetics of carbon nanotubes using intrinsic near-infrared fluorescence. *Proc. Natl. Acad. Sci. U.S.A.* **103**, 18882–18886.

Cox, C. (1991) Chromated copper arsenate. *J. Pest. Reform* **11**, 2–6.

Domingos, R.F., Baalousha, M.A., Ju-Nam, Y., Reid, M.M., Tufenkji, N., Lead, J.R., Leppard, G.G. & Wilkinson, K.J. (2009) Characterizing manufactured nanoparticles in the environment: multimethod determination of particle sizes. *Environ. Sci. Technol.* **43**, 7277–7284.

Dynes, J.J., Lawrence, J.R., Korber, D.R., Swerhone, G.D.W., Leppard, G.G. & Hitchcock, A.P. (2006b) Quantitative mapping of chlorhexidine in natural river biofilms. *Sci. Total Environ.* **369**, 369–383.

Dynes, J.J., Lawrence, J.R., Korber, D.R., Swerhone, G.D.W., Leppard, G.G. & Hitchcock, A.P. (2009) Morphological and biochemical changes in pseudomonas fluorescens biofilms induced by sub-lethal exposure to antimicrobial agents. *Can. J. Microbiol.* **55**, 163–178.

Dynes, J.J., Tyliszczak, T., Araki, T., Lawrence, J.R., Swerhone, G.D.W., Leppard, G.G. & Hitchcock, A.P. (2006a) Speciation and quantitative mapping of metal species in microbial biofilms using scanning transmission X-ray microscopy. *Environ. Sci. Technol.* **40**, 1556–1565.

Eickhoff, E.M., Obst, M., Schröder, C., *et al.* (2014) Nickel partitioning in biogenic and abiogenic ferrihydrite: the influence of silica and implications for ancient environments. *Geochim. Cosmochim. Acta* **140**, 65–79.

Felten, A., Bittencourt, C., Pireaux, J.-J., Reichelt, M., Mayer, J., Hernandez Cruz, D. & Hitchcock, A.P. (2007) Individual multi-wall carbon nanotubes spectroscopy by scanning transmission X-ray microscopy. *Nanoletters* **7**, 2435–2440.

Felten, A., Hody, H., Bittencourt, C., Pireaux J.-J., Hernandez Cruz, D. & Hitchcock, A.P. (2006) Scanning transmission X-ray microscopy of

isolated multi-wall carbon nanotubes. *Appl. Phys. Lett.* **89**, 093123-(1–3).

Gao, J., Youn, S., Hovsepyan, A., Llandeza, V.L., Wang, Y., Bitton, G. & Bonzongo, J.-C.J. (2009 Dispersion and toxicity of selected manufactured nanomaterials in natural river water samples: effects of water chemical composition. *Environ. Sci. Technol.* **43**, 3322–3328.

Gianoncelli, A., Kaulich, B., Alberti, R., Klatka, T., Longoni, A., De Marco, A., Marcello, A. & Kiskinova, M. (2009) Simultaneous soft X-ray transmission and emission microscopy. *Nucl. Instrum. Methods Phys. Res. A* **608**, 195–199.

Gianoncelli, A., Marmorato, P., Ponti, J., *et al.* (2013) Interaction of magnetic nanoparticles with U87MG cells studied by synchrotron radiation X-ray fluorescence techniques. *X-Ray Spectrom.* **42**, 316–320.

Giepmans, B.N.G. (2008) Bridging fluorescence microscopy and electron microscopy. *Histochem. Cell Biol.* **130**, 211–217.

Gomes, W.C.M., Neto, A.D.W., Pimentel, P.M., Melo, D.M.D. & Silva, F.R.G.E. (2013) An in situ X-ray absorption spectroscopy study of copper nanoparticles in microemulsion. *Colloids Surf. A* **426**, 18–25.

Graf, C., Meinke, M., Cao, Q., *et al.* (2008) High resolution detection of single nanoparticles in human skin by STXM. *J. Biomed. Opt.* **14**, 021015-(1–9).

Gu, W., Wang, H. & Wang, K. (2014) Nickel L-edge and K-edge X-ray absorption spectroscopy of non-innocent $Ni[S_2C_2(CF_3)_2]_{2n}$ series (n = −2, −1, 0): direct probe of nickel fractional oxidation state changes. *Dalton Trans.* **43**, 6406–6413.

Handy, R.H., Owen, R. & Valsami-Jones, E. (2008) The ecotoxicology of nanoparticles and nanomaterials: current status, knowledge gaps, challenges, and future needs. *Ecotoxicology* **17**, 315–325.

Henderson, G.S., Liu, X. & Fleet, M.E. (2002) A Ti L-edge X-ray absorption study of Ti-silicate glasses. *Phys. Chem. Miner.* **29**, 32–42.

Hernandez-Viezcas, J.A., Castillo-Michel, H., Andrews, J.C. *et al.* (2013) In situ mapping of X-ray fluorescence mapping and speciation of CeO_2 and ZnO nanoparticles in soil cultivated soybean (Glycine max). *ACS Nano* **7**, 1415–1423.

Hitchcock, A.P. (2012) Soft X-ray imaging and spectromicroscopy. *Handbook on Nanoscopy* (ed. by T. VanGustaaf, D. Van Dirk & S.J. Pennycook), Chap. 22, vol. **II**, pp 745–791. Wiley, Weinheim, Germany.

Hitchcock, A.P. (2014) aXis2000 is written in Interactive Data Language (IDL). It is available free for noncommercial use from http://unicorn.mcmaster.ca/aXis2000.html (accessed 30 June 2014).

Hitchcock, A.P., Dynes, J.J., Johansson, G.A., Wang, J. & Botton, G. (2008a) Comparison of NEXAFS microscopy and TEM-EELS for studies of soft matter. *Micron* **39** 741–748.

Hitchcock, A.P., Dynes, J.J., Lawrence, J.R., Obst, M., Swerhone, G.D.W., Korber, D.R. & Leppard, G.G. (2009) Soft X-ray spectromicroscopy of nickel sorption in a natural river biofilm. *Geobiology* **7**, 432–453.

Hitchcock, A.P., Johansson, G.A., Mitchell, G.E., Keefe, M. & Tyliszcak, T. (2008b) 3D chemical imaging using angle-scan tomography in a soft X-ray scanning transmission X-ray microscope. *Appl. Phys. A* **92**, 447–452.

Hitchcock, A.P. Obst, M., Wang, J., Lu, Y.S. & Tyliszczak, T. (2012) Advances in the detection of As in environmental samples using low energy X-ray fluorescence in a scanning transmission X-ray microscope: arsenic immobilization by an Fe(II)-oxidizing freshwater bacteria. *Environ. Sci. Technol.* **46**, 2821–2829.

Huang, C.P., Cha, D.K. & Ismat, S.S. (2005) Progress report: short-term chronic toxicity of photocatalytic nanoparticles to bacteria, algae, and zooplankton. EPA Grant Number: R831721. Available at: http://cfpub.epa.gov/ncer_abstracts/index.cfm/fuseaction/display.abstractDetail/abstract/7384/report/0 (accessed 15 July 2014).

Jahn, K.A., Barton, D.A., Kobayashi, K., Ratinac, K.R., Overall, R. L. & Braet, F. (2012) Correlative microscopy: providing new understanding in the biomedical and plant sciences. *Micron* **43**, 565–582.

Johansson, G.A., Dynes, J.J., Hitchcock, A.P., Tyliszczak, T., Swerhone, G.D.W. & Lawrence, J.R. (2006) Chemically sensitive 3D imaging at sub 100 nm spatial resolution using tomography in a scanning transmission X-ray microscope. *Developments in X-Ray Tomography V* (ed. by Bonse U.). In *Proc. SPIE*, **6318**, 1I-(1–9).

Johansson, G.A., Tyliszczak, T., Mitchell, G.E., Keefe, M. & Hitchcock, A.P. (2007). Three dimensional chemical mapping by scanning transmission X-ray spectromicroscopy. *J. Synchrotron Radiat.* **14**, 395–412.

de Jonge, M.D., Holzner, C., Baines, S.B., *et al.* (2010) Quantitative 3D elemental microtomography of *Cyclotella meneghiniana* at 400-nm resolution. *Proc. Natl. Acad. Sci. U.S.A.* **107**, 15676–15680.

Kaindl, G., Kalkowski, G., Brewer, W.D., Perscheid, B. & Holtzberg, F. (1984) M-edge X-ray absorption-spectroscopy of 4f instabilities in rare-earth systems. *J. Appl. Phys.* **55**, 1910–1915.

Kalirai, S.S., Bazylinski, D.A. & Hitchcock, A.P. (2013) Anomalous magnetic orientations of magnetosome chains in a magnetotactic bacterium: *Magnetovibrio Blakemorei* strain MV-1. *PLoS One* **8** e53368-(1–7).

Kalirai, S.S., Lam, K.P., Bazylinski, D., Lins, U. & Hitchcock, A.P. (2012) Examining the chemistry and magnetism of magnetotactic bacterium *Candidatus Magnetovibrio blakemorei* strain MV-1 using scanning transmission X-ray microscopy. *Chem. Geol.* **300–301**, 14–23.

Kam, N.W. O'Conell, M., Wisdom, J.A. & Dai, H. (2005) Carbon nanotubes as multifunctional biological transporters and near infrared agents for selective cancer cell destruction. *Proc. Natl. Acad. Sci. U.S.A.* **102**, 11600–11605.

Kang, S., Mauter, M.S. & Elimelech, M. (2009) Microbial cytotoxicity of carbon-based nanomaterials: implications for river water and wastewater effluent. *Environ. Sci. Technol.* **43**, 2648–2653.

Kasemets, K., Ivask, A., Dubourguier, H.-C. & Kahru, A. (2009) Toxicity of nanoparticles of ZnO, CuO and TiO2 to yeast *Saccharomyces cerevisiae*. *Toxicol. In Vitro* **23**, 1116–1122.

Kaznatcheev, K.V., Karunakaran, C., Lanke, U.D., Urquhart, S.G., Obst, M. & Hitchcock, A.P. (2007) Soft X-ray spectromicroscopy beamline at the CLS: commissioning results. *Nucl. Instrum. Methods Phys. Res. A* **582**, 96–99.

Kilcoyne, A.L.D, Steele, W.F., Fakra, S., *et al.* (2003) Interferometrically controlled scanning transmission microscopes at the advanced light source. *J. Synchrotron Radiat.* **10**, 125–136.

Kim, W.J., Usrey, M.L. & Strano, M.S. (2007) Selective functionalization and free solution electrophoresis of single-walled carbon nanotubes: separate enrichment of metallic and semiconducting SWNT. *Chem. Mater.* **19**, 1571–1576.

Lam, K.P., Hitchcock, A.P., Obst, M., Lawrence, J.R., Swerhone, G.D.W., Leppard, G.G., Tyliszczak, T., Karunakaran, C., Wang, J., Kaznatcheev, K., Bazylinski, D.A. & Lins, U. (2010) X-ray magnetic circular dichroism of individual magnetosomes by scanning transmission X-ray microscopy, *Chem. Geol.* **270**, 110–116.

Lawrence, J.R., Chenier, M.R., Roy, R., Beamier, D., Fortin, N., Swerhone, G.D.W., Neu, T.R. & Greer, C.W. (2004) Microscale and molecular assessment of impacts of nickel, nutrients and oxygen level on structure

and function of river biofilm communities. *Appl. Environ. Microbiol.* **70**, 4326–4339.

Lawrence, J.R., Dynes, J.J., Korber, D.R., Swerhone, G.D.W. & Leppard, G.G. (2012) Monitoring the fate of copper nanoparticles in river biofilms using scanning transmission X-ray microscopy (STXM), *Chem. Geol.* **329**, 18–25.

Lawrence, J.R. & Hitchcock, A.P. (2011) Synchrotron-based X-ray and FTIR absorption spectromicroscopies of organic contaminants in the environment. *Biophysico-Chemical Processes of Anthropogenic Organic Compounds in Environmental Systems* (ed. by B.N. Xing, N. Senesi & P.M. Huang), pp. 341–368. International Union of Pure and Applied Chemistry Books Series, John Wiley & Sons, New Jersey, USA.

Lawrence, J.R., Scharf, B., Packroff, G. & Neu, T.R. (2002) Microscale evaluation of the effects of grazing by invertebrates with contrasting feeding modes on river biofilm architecture and composition. *Microb. Ecol.* **44**, 199–207.

Lawrence, J.R., Swerhone, G.D.W., Dynes, J.J., Hitchcock, A.P & Korber, D.R. (2014) Complex organic corona formation on carbon nanotubes reduces microbial toxicity by suppressing reactive oxygen species production. *Environ. Toxicol. Chem.* in submission.

Lawrence, J.R., Swerhone, G.D.W., Leppard, G.G., Araki, T., Zhang, X., West, M.M. & Hitchcock, A.P. (2003) Scanning transmission X-ray, laser scanning, and transmission electron microscopy mapping of the exopolymeric matrix of microbial biofilms. *Appl. Environ. Microbiol.* **69**, 5543–5554.

Li, K.G., Chen, Y., Zhang, W., Pu, Z.C., Jiang, L. & Chen, Y.S. 2012. Surface interactions affect the toxicity of engineered metal oxide nanoparticles toward Paramecium. *Chem. Res. Toxicol.* **25**, 1675–1681.

Lerotic, M., Jacobsen, C., Schäfer, T. & Vogt, S. (2004) Cluster analysis of soft X-ray spectromicroscopy data. *Ultramicroscopy* **100**, 35–44.

Lombi, E., de Jonge, M.D., Donner, E., Kopittke, P.M., Howard, D.L., Kirkham, R., Ryan, C.G. & Paterson, D. (2011) Fast X-ray fluorescence microtomography of hydrated biological samples. *PLOS One* **6**, e20626.

Lowry, G.V., Gregory, K.B., Apte, S.C. & Lead, J.R. (2012) Transformations of nanomaterials in the environment. *Environ. Sci. Technol.* **46**, 6893−6899.

Lynch, I. & Dawson, K.A. (2008) Protein-nanoparticle interactions. *Nano Today*, **3**, 40−47.

Marmorato, P., Ceccone, G., Gianoncelli, A., *et al.* (2011) Cellular distribution and degradation of cobalt ferrite nanoparticles in Balb/3T3 mouse fibroblasts. *Toxicol. Lett.* **207**, 128–136.

Miller, R.J., Bennett, S., Keller, A.A., Pease, S. & Lenihan, H.S. (2012) TiO_2 nanoparticles are phototoxic to marine phytoplankton. *PLoS ONE* **7**, e30321.

Miyata, Y., Yanagi, K., Maniwa, Y. & Kataura, H. (2008) Optical evaluation of the metal-to-semiconductor ratio of single-wall carbon nanotubes. *J. Phys. Chem. C* **112**, 13187–13191.

Muehe, E.M., Obst, M., Hitchcock, A.P., *et al.* (2013) Fate of Cd during microbial Fe(III) mineral reduction by a novel and Cd-tolerant Geobacter species. *Environ. Sci. Technol.* **47**, 14099–14109.

Mueller, N.C. & Nowack, B. (2008) Exposure modeling of engineered nanoparticles in the environment. *Environ. Sci. Technol.* **42**, 4447–4453.

Najafi, E., Felten, A., Douhard, B., Hernandez Cruz, D., Obst, M., Hitchcock, A.P. & Pireaux, J.-J. (2008) Polarization dependence of the C 1s X-ray absorption spectra of individual multi-walled carbon nanotubes. *Small* **4**, 2279–2285.

Najafi, E., Hitchcock, A.P., Rossouw, D. & Botton, G.A. (2012) Mapping defects in a carbon nanotube by momentum transfer dependent electron energy loss spectromicroscopy. *Ultramicroscopy* **113**, 158–164.

Najafi, E. Wang, J., Hitchcock, A.P., Guan, J., Denommee, S. & Simard, B. (2010) Characterization of single-walled carbon nanotubes by scanning transmission X-ray spectromicroscopy: purification, order and dodecyl functionalization. *J. Am. Chem. Soc.* **132**, 9020–9029.

Neu, T.R., Manz, B., Volke, F., Dynes, J.J., Hitchcock, A.P. & Lawrence, J.R. (2010) Advanced imaging techniques for assessment of structure, composition and function in biofilm systems. *FEMS Microbiol. Ecol.* **72**, 1–21.

Novak, S., Drobne, D., Golobic, M., *et al.* (2013) Cellular internalization of dissolved cobalt ions from ingested $CoFe_2O_4$ nanoparticles: in vivo experimental evidence. *Environ. Sci. Technol.* **47**, 5400–5408.

Obst, M., Wang, J. & Hitchcock, A.P. (2009) Soft X-ray spectrotomography study of cyanobacterial biomineral nucleation. *Geobiology* **7**, 577–591.

Park, B., Donaldson, K., Duffin, R., *et al.* (2008) Hazard and risk assessment of a nanoparticulate cerium oxidebased diesel fuel additive – a case study. *Inhal. Toxicol.* **20**, 547–566.

Patterson, G., Davidson, M., Manley, S. & Lippincott-Schwartz, J. (2010) Super resolution imaging using single-molecule localization. *Annu. Rev. Phys. Chem.* **61**, 345–367.

Petersen, E.J. & Henry, T.B. (2011) Methodological considerations for testing the ecotoxicity of carbon nanotubes and fullerenes. *Environ. Toxicol. Chem.* **31**, 60–72.

Petersen, E.J., Zhang, L., Mattison, N., *et al.* (2011) Potential release pathways, environmental fate, and ecological risks of carbon nanotubes. *Environ. Sci. Technol.* **45**, 9837–9856.

Pitticharoenphun, S., Siller, L., Lemloh, M-L., *et al.* (2012) Agglomeration of silver nanoparticles in Sea Urchin, *Int. J. Environ. Pollut. Remediat.* **1**, 46–52.

Porter, A.E, Grass, M., Muller, K., Skepper, J.N., Midgley, P.A. & Welland, M. (2007) Direct imaging of single-walled carbon nanotubes in cells. *Nat. Nanotechnol.* **2**, 713–717.

Quigg, A., Chin, W-C., Chen, C-S., *et al.* (2013) Direct and indirect toxic effects of engineered nanoparticles on algae: role of natural organic matter. *ACS Sustain. Chem. Eng.* **1**, 686–702.

Rajendran, P., Muthukrishnan, J. & Gunasekaran, P. (2002) Current perspectives in nickel bioremediation strategies. *Indian J. Microbiol.* **42**, 1–9.

Rao, A.M., Richter, E., Bandow, S., *et al.* (1997) Diameter selective Raman scattering from vibrational modes in carbon nanotubes. *Science* **275**, 187–191.

Ren, G., Hu, D., Cheng, E.W.C., Vargas-Reus, M.A., Reip, P. & Allaker, R.P. (2009) Characterisation of copper oxide nanoparticles for antimicrobial applications. *Int. J. Antimicrob. Agents* **33**, 587–590.

Rossouw, D., Botton, G.A., Najafi, E., Lee, V. & Hitchcock, A.P. (2012) Metallic and semiconducting single-walled carbon nanotubes: differentiation individual SWCNT by their carbon 1s spectra. *ACS Nano* **6**, 10965–10972.

Schmid, G., Zeitvogel, F., Hao, L., *et al.* (2014) Synchrotron-based chemical nano-tomography of microbial cell-mineral aggregates in their natural, hydrated state. *Microsc. Microanal.* **20**, 531–536.

Servin, A.D., Morales, M.I., Castillo-Michel, H., *et al.* (2013) Synchrotron verification of TiO2 accumulation in cucumber fruit: A possible

pathway of TiO_2 nanoparticle transfer from soil into the food chain. *Environ. Sci. Technol.* **47**, 11592–11598.

Shah, V., Shah, S., Shah, H., *et al.* (2012) Antibacterial activity of polymer coated cerium oxide nanoparticles. *PLoS ONE* **7**(10), e47827.

Shi, D., Guo, Y., Dong, Z., Lian, J., Wang, W., Liu, G., Wang, L. & Ewing, R.C. (2007) Quantum dot activated luminescent carbon nanotubes via a nanoscale surface functionalization for *in vivo* imaging. *Adv. Mater.* **19**, 4033–4037.

Smythe, D.J., Brenan, J.M., Bennett, N.R., Regier, T. & Henderson, G.S. (2013) Quantitative determination of cerium oxidation states in alkali-aluminosilicate glasses using $M_{4,5}$-edges XANES. *J. Non Cryst. Solids* **378**, 258–264.

Thill, A., Zeyons, O., Spalla, O., Chauvat, F., Rose, J., Auffan, M. & Flank, A.M. (2006) Cytotoxicity of CeO_2 nanoparticles for *Escherichia coli* physico-chemical insight of the cytotoxicity mechanism. *Environ. Sci. Technol.* **40**, 6151–6156.

Tiede, K., Tear, S.P., David, H. & Boxall, A.B.A. (2009) Imaging of engineered nanoparticles and their aggregates under fully liquid conditions in environmental matrices. *Water Res.* **43**, 3335–3343.

Thieme, J., Gleber, S.C., Guttmann, P., Prietzel, J., McNulty, I. & Coates, J. (2008) Microscopy and spectroscopy with X-rays for studies in the environmental sciences. *Mineral. Mag.* **72**, 211–216.

Thieme, J., Sedlmair, J., Gleber, S.C. Prietzel, J., Coates, J., Eusterhues, K., Abbt-Braun, G. & Salome, M. (2010) X-ray spectromicroscopy in soil and environmental sciences. *J. Synchrotron Radiat.* **17** 149–157.

Van Hoecke, K., Quik, J.T.K., Mankiewicz-Boczek, J., *et al.* (2009) Fate and effects of CeO_2 nanoparticles in aquatic ecotoxicity tests. *Environ. Sci. Technol.* **43**, 4537–4546.

Wang, H., Patil, D.S., Gu, W., Jacquamet, L., Friedrich, S., Funk, T. & Cramer, S.P. (2001) L-edge X-ray absorption spectroscopy of some Ni enzymes: probe of Ni electronic structure. *J. Electron Spectros. Relat. Phenomena* **114–116**, 855–863.

Wang, H.-X., Ralston, C.Y., Patil, D.S., *et al.* (2000) Nickel L-edge soft X-ray spectroscopy of nickel—iron hydrogenases and model compounds – evidence for high-spin nickel(ii) in the active enzyme. *J. Am. Chem. Soc.* **122**, 10544–10552.

Wang, J., Botton, G.A., West, M.M. & Hitchcock, A.P. (2009a) Quantitative evaluation of radiation damage to polyethylene terephthalate by soft X-rays and high energy electrons. *J. Phys. Chem. B* **113**, 1869–1876.

Wang, J., Morin, C., Li, L., Hitchcock, A.P., Zhang, X. Araki, T., Doran, A. & Scholl, A. (2009b) Radiation damage in soft X-ray microscopy. *J. Electron Spectros. Relat. Phenomena* **170** 25–36.

Wild, E. & Jones, K. (2009) Novel method for the direct visualization of in vivo nanomaterials and chemical interactions in plants. *Environ. Sci. Technol.* **43**, 5290–5294.

Wild, E. & Jones, K.C. (2007) Seeing chemicals in environmental samples. *Environ. Sci. Technol.* **41**, 5935–5938.

de la Zerda, A. & Gambhir, S.S. (2007) Keeping tabs on nanocarriers. *Nat. Nanotechnol.* **2**, 745–746.

Zhang, H., Wang, J., Pan, X., Hu, Y.F. & Bao, X. (2012) Local structure of titania decorated double-walled carbon nanotube characterized by scanning transmission X-ray microscopy. *J. Chem. Phys.* **136**, 174701-(1–6).

Zhou, K., Wang, R., Xu, B. & Li, Y. (2006) Synthesis, characterization and catalytic properties of CuO nanocrystals with various shapes. *Nanotechnol.* **17**, 3939–3943.